Advanced Steel Construction – Vol. 20 No. 3 (2024) 266–279
DOI:10.18057/IJASC.2024.20.3.6

BEHAVIOR AND DESIGN OF COLD-FORMED SQUARE AND RECTANGULAR HOLLOW SECTIONS BASED ON EFFECTIVE PLASTIC WIDTH METHOD

Shuo Ren [1], Xin Cheng [1, *], Xia-Xin Wang [2] and Li-Jun Zhuang [3]

[1] *Department of Civil Engineering, Taiyuan University of Technology, Taiyuan, 030024, China*
[2] *School of Civil Engineering, Southeast University, Nanjing, 210096, China*
[3] *China Shanxi Sijian Group Co., Ltd., Taiyuan, 030006, China*
** (Corresponding author: E-mail: xchengtyut@126.com)*

ABSTRACT

Due to the rapid development of cold-forming technology, the application of cold-formed steel members with square hollow sections (SHS) and rectangular hollow sections (RHS) in constructing steel structures is increasingly developing. For practical application, it is of great significance to study the ultimate behavior of cold-formed SHS and RHS steel tubes with different plate thicknesses systematically. In this paper, finite element models considering initial geometric defects, residual stress, and cold-formed effect were established and validated against available test data. Parametric analysis was then conducted considering various width-to-thickness ratios of flange and web and axial force ratios. The influences of the parameters on the ultimate capacity, failure mechanism, and stress development were carefully explored using the results of parametric analysis. The effective plastic width method (EPM) was introduced to calculate the ultimate capacity, taking strain hardening, interactive effect of the plates, and local buckling into account. Finally, the accuracy of EPM was verified through comparison with current specifications and parametric analysis results.

ARTICLE HISTORY

Received: 26 July 2023
Revised: 22 February 2024
Accepted: 23 February 2024

KEYWORDS

Ultimate capacity;
Cold-formed SHS and RHS;
Effective plastic width method;
Parametric analysis;
Interactive effect of plates

1. Introduction

Cold-formed square hollow sections (SHS) and rectangular hollow sections (RHS) are widely utilized due to their excellent rigidity, corrosion resistance, fire protection, and manufacturing efficiency [1]. With improvement in the cold-forming process, the thickness of cold-formed SHS and RHS has been significantly extended, even reaching 25 mm [2-4]. Therefore, the research on the bearing capacity of cold-formed SHS and RHS steel members has recently received extensive attention, especially on those members composed of relatively thick sections [5-9].

Numerous researchers have engaged in studies to validate the accuracy of the ultimate capacities computed for cold-formed SHS and RHS members according to the Chinese design standard GB50018-2002 [10] (abbreviated as GB50018) and the European code EC3-part1-1 [11] (abbreviated as EC3). It is noted that the current GB50018 is applicable to members with a thickness ranging from 2 to 6 mm. Wu et al. [12] and Shen [13] demonstrated that the predictions from GB50018 for the compressive capacity of the members within the specified thickness range were conservative. Li et al. [14], Wen et al. [15], and Hu et al. [16] indicated that the applicability of GB50018 to steel members with a thickness beyond 6 mm was still controversial. Regarding EC3, Wang et al. [17] and Ma et al. [18-20] showed that EC3 was risky for slender sections but prudent for compact ones. Nseir [21] also reported that the section classification limitations in EC3 were not directly applicable to cold-formed steel members. Moreover, the calculation method of EC3 would lead to discontinuity in the bearing capacity of the sections classified as classes 2 and 3 by neglecting the partial plastic development in class 3 sections. Therefore, conducting a thorough study on the ultimate bearing capacity of cold-formed SHS and RHS steel members is necessary.

Many researchers have investigated the bearing capacity of cold-formed SHS and RHS steel tubes experimentally and numerically. For the ultimate compressive capacity, Hou [22] conducted experimental tests and finite element (FE) simulations to obtain the axial compressive capacity of thick-walled columns, and proposed modified formulas for calculating the bearing capacity. Li et al. [14] carried out reliability analysis based on experimental tests and FE analyses, subsequently recommending appropriate partial resistance factors and strength design values for Q235 and Q345 steels. Yao et al. [23] stated that GB50018 could be used to design members with a plate thickness of less than 2 mm. In another work, Wen et al. [15] conducted axial compression tests on thick-walled members, proposed methods for calculating the section yield strength considering the cold bending effect, and demonstrated that GB50018 was conservative. Through experimentation and numerical simulation, Ma et al. [18, 19] proposed an improved direct strength method to calculate the ultimate bearing capacity for high-strength members.

The ultimate capacity of members under combined compression and bending is primarily based on testing or numerical simulation considering eccentric compression. Nseir [21] conducted experiments and FE studies on cold-formed SHS and RHS steel tubes under various loading conditions and proposed an overall interaction method. Yun and Gardner [24] developed a continuous strength method suitable for thick-walled members. Deng [25] also proposed a continuous strength method for thin-walled members. Ma et al. [20, 26] studied the bearing capacity of high-strength members under eccentric compression and revealed that the predictions of the current specifications were 13%–21% lower on average. In addition, Li et al. [27] experimentally examined high-strength, thin-walled members under axial compression and showed that the influence of the interactions of the plates on the compressive capacity should not be ignored. Chen et al. [28, 29] proposed a formula for calculating the constraint coefficient of the plates and critical stress when reaching buckling. Wu et al. [12] determined the stress redistribution of the compressive plate at the ultimate moment and analyzed the plate group effect after the buckling of the rectangular tube. However, these calculations were complex and not easy to use.

Chen et al. [30] introduced the effective plastic width method (EPM) to estimate the ultimate capacity of H-section members subjected to combined compression and bending around the strong axis. This approach was later expanded by Cheng et al. [31] to calculate the bearing capacities of H-section members with combined compression and bending. Shi et al. [32] then utilized EPM to assess the bearing capacity of cold-formed SHS members. EPM operates on the premise that the entire effective section can achieve plasticity, enabling the calculation of the ultimate capacity according to the given stress distribution of the section at the limit state. Compared with other methods, EPM can better consider the influence of interactive effect, local buckling of plates and the strain hardening of section. Furthermore, EPM's applicability is not confined by the classification of sections, leading to more precise and straightforward calculations. Consequently, employing EPM for calculating the ultimate capacity of cold-formed SHS and RHS steel pipes is considered practical and effective.

Considering the research conducted so far, the study of the bearing capacities of cold-formed SHS and RHS steel tubes under compression and combined compression and bending is found to be inadequate. The current computational methods suffer from inadequate consideration of plastic development of section and strain hardening, as well as the interactive effect of plates, resulting in inaccuracies in bearing capacity calculations. Therefore, this paper aims to propose a comprehensive method for calculating the ultimate capacity of members subjected to combined compression and bending based on EPM, taking into account the above aspects.

This paper studies the ultimate capacity of cold-formed SHS and RHS steel members under axial compression and combined compression and

bending, covering different width-to-thickness ratios of the flange and web. The failure mechanisms of members under axial compression and combined compression and bending are summarized, and the stress development law during the loading process is revealed. The EPM for calculating the ultimate capacity taking into account the interactive effects of the plates is also established.

2. Establishment and verification of FE models

2.1. Establishment of FE models

The detailed modeling procedure can be referred to Shi et al. [32]. Fig. 1 depicts the FE simulation of the members considering three loading modes, where *w* and Δ respectively represents the axial and lateral displacement of the column top, respectively, and *l* represents the column length. In this paper, the eccentric compression loading mode (Fig. 1b) is used to verify the developed FE model, while the cantilever bending mode (Fig. 1c) is used for parametric analysis. The geometric definition of the section is shown in Fig. 2. The element type of the FE model is S4R shell element, and the mesh size settlement and boundary conditions are illustrated in Fig. 3. In parametric analysis, the first buckling mode (the most unfavorable mode) with an odd number of buckling waves along the length of the column is selected to simulate the initial geometric imperfection, and the amplitude of the defect is taken as min (B/200, H/200) [33]. During the FE model verification, the measured data on material properties and residual stresses are incorporated as inputs. The material model proposed by Gardner and Yun [34] is employed for conducting parametric studies. This model assigns distinct stress-strain characteristics to the corners and flat plates of a structure respectively, deliberately excluding the extension of corner material characteristics. It enhances the Ramberg-Osgood model by integrating findings from extensive material property tests on various cold-formed sections with a range of yield strengths and thicknesses. It is adept at accounting for the diverse strengths, thicknesses, and shapes of cold-formed steels, as well as the cold-formed effect of sections [2,24,32], as illustrated in Fig. 4. For parametric analysis, the longitudinal bending residual stress model proposed by Somodi and Kovesd [38] is applied to assess the impact of residual stress on the component behavior [36,37], as depicted in Fig. 5. This model, validated by tests on both thin-wall and thick-wall cold-formed steel, is noted for its broad applicability and conservative nature due to its assumption of significant longitudinal residual stress amplitudes.

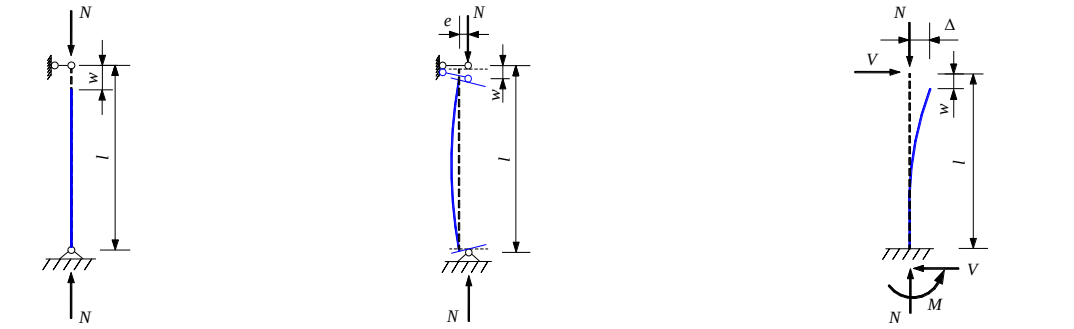

(a) Axial compression (b) Eccentric compression (c) Combined compression and bending

Fig. 1 The loading modes

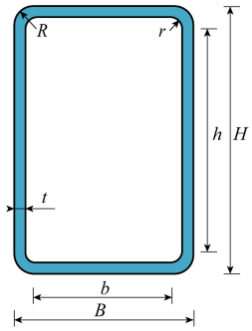

Fig. 2 The geometric dimensions of the section

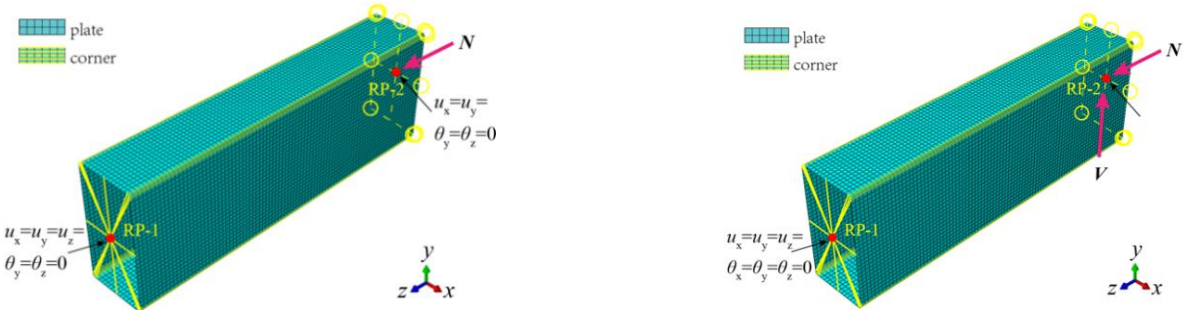

(a) Members subjected to axial compression and eccentric compression (b) Cantilever members subjected to combined compression and bending

Fig. 3 Mesh generation and boundary conditions

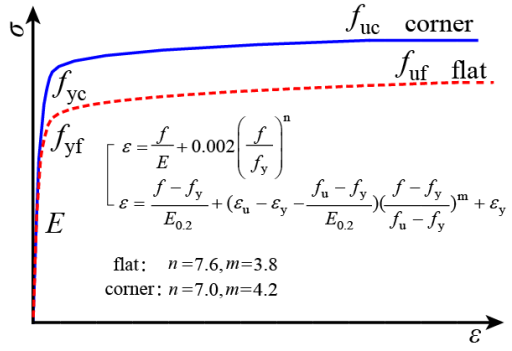

Fig. 4 The material properties

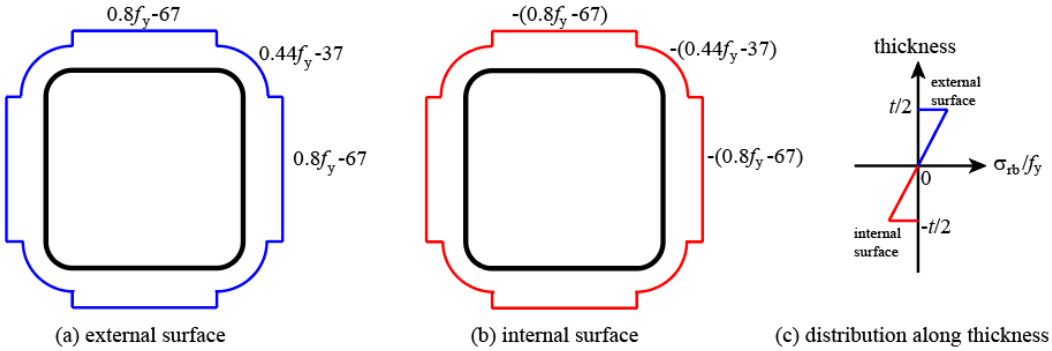

Fig. 5 The residual stress model

2.2. Verification of FE model

In this paper, existing experimental data were summarized to verify the FE model. The basic information of the test specimens is shown in Table 1, where $N_{u,test}$ and $N_{u,FE}$ are the ultimate capacities obtained by test and FE simulation respectively. The failure modes, load-displacement curves (N-w) and ultimate capacity of the FE model were extracted and compared with the test results, depicted in Figs. 6–8. The comparison results indicate that the FE model can accurately simulate the failure modes, ultimate capacities, and overall trend of the members' behavior throughout the curve. Slight differences in N-w curves can result from dimensional errors and alignment errors, among other factors. Thus, the model could accurately simulate the compressive and bending behavior of cold-formed SHS and RHS members.

Table 1
Basic information of specimens

Reference	Specimen number	Steel	B (mm)	H (mm)	t (mm)	l (mm)	e (mm)	$N_{u,test}$ (kN)	$N_{u,FE}$ (kN)	$N_{u,test}$ / $N_{u,FE}$
Nseir [21]	Stub_200 × 100 × 4	S355	100	201	3.7	600	0	761	741	0.974
	Stub_220 × 120 × 6		120	221	5.9	600	0	1648	1627	0.987
	Stub_200 × 200 × 5		201	200	4.7	600	0	1296	1307	1.008
	Stub_200 × 200 × 6		200	200	5.9	600	0	1957	1934	0.988
	LC2_200 × 200 × 5		200	201	4.9	700	77	816	816	1.004
	LC2_200 × 200 × 6		200	200	6.1	700	72	1179	1150	0.976
	LC2_200 × 100 × 4		101	200	4.0	700	60	597	613	1.027
	LC2_220 × 120 × 6		121	219	6.3	700	67	1160	1133	0.977
	LC4_200 × 100 × 4		200	101	4.1	700	35	471	459	0.975
	LC4_220 × 120 × 6		220	120	6.2	700	40	972	963	0.991
Hou [22]	SC1	Q345	140	140	10.0	820	0	2650	2631	0.993
	SC2	Q345	150	150	8.0	850	0	2466	2547	1.033
	SC3	Q235	200	200	8.0	1000	0	2807	2754	0.981
	SC4	Q235	200	200	12.0	1000	0	3606	3824	1.040
	SC5	Q345	200	200	16.0	1000	0	5873	5876	1.000
Gardner et al. [39]	SHS-100-100-4	Q235	101	101	3.6	405	0	660	659	0.998
	SHS-60-60-3		60	60	2.8	245	0	249	247	0.992
	RHS-60-40-4		60	40	4.0	245	0	370	349	0.943
	SHS-40-40-4		40	40	3.8	165	0	256	245	0.957
	SHS-40-40-3		40	40	2.8	165	0	224	215	0.960

Reference	Specimen number	Steel	B (mm)	H (mm)	t (mm)	l (mm)	e (mm)	$N_{u,test}$ (kN)	$N_{u,FE}$ (kN)	$N_{u,test}$ / $N_{u,FE}$
Hu et al. [40]		Q345	250	250	9.3	910	0	3600	3550	0.986
			250	250	9.2	910	0	3725	3905	1.048
			250	250	9.2	910	0	3650	3588	0.983
			300	200	9.2	909	0	3490	3586	1.028
			300	200	9.3	912	0	3350	3257	0.972
			300	200	9.2	909	0	3340	3257	0.975
Sun et al. [41]		690	152	152	8.0	498	0	3734	3757	1.006
		350	152	152	13.0	500	0	3873	3817	0.985
		350	152	152	6.4	600	0	1711	1739	1.017
Chen [42]		Q235	250	250	9.0	500	0	2820	2874	1.019
			300	200	8.0	500	0	2430	2344	0.965
Gao [43]		Q235	250	100	8.0	500	0	1860	1886	1.014
			200	200	8.0	500	0	2320	2225	0.959

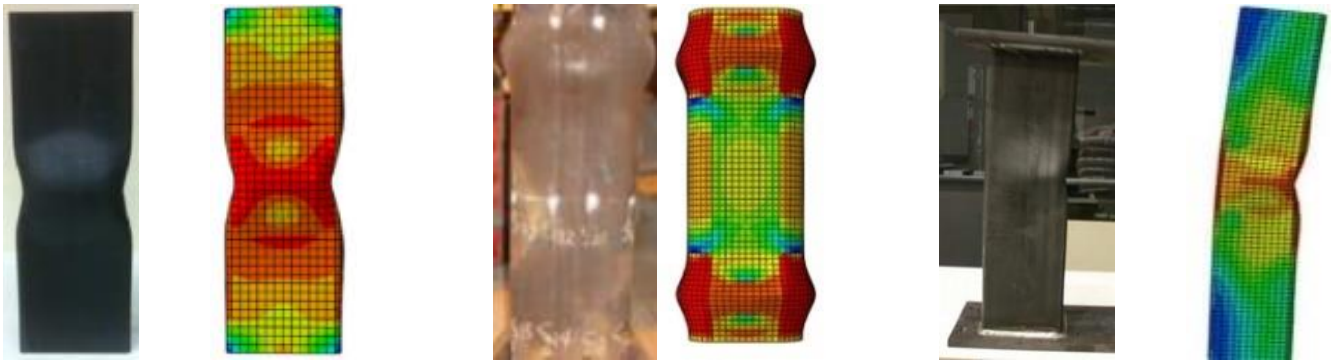

(a) Stub_200 × 200 × 5 (b) SC5 (c) LC2_200 × 200 × 5

Fig. 6 Comparisons of failure modes of typical members [21,22]

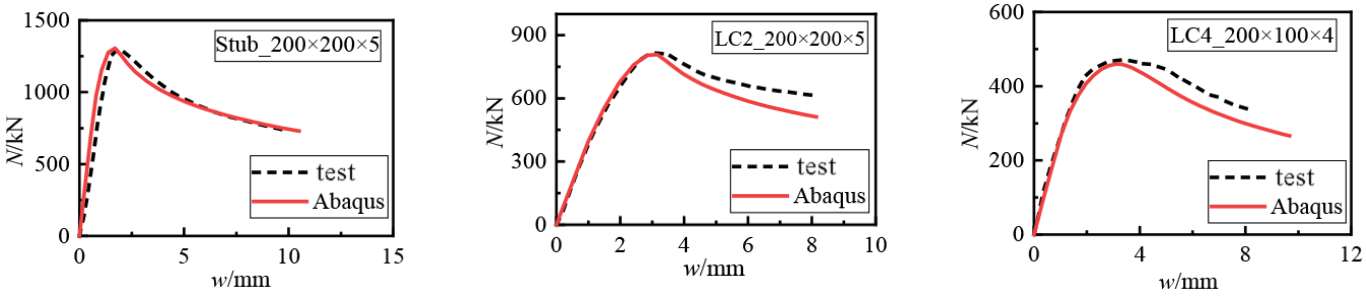

(a) Stub_200 × 200 × 5 [21] (b) LC2_200 × 200 × 5 [21] (c) LC4_200 × 100 × 4 [21]

Fig. 7 Comparison results of *N*-*w* curves

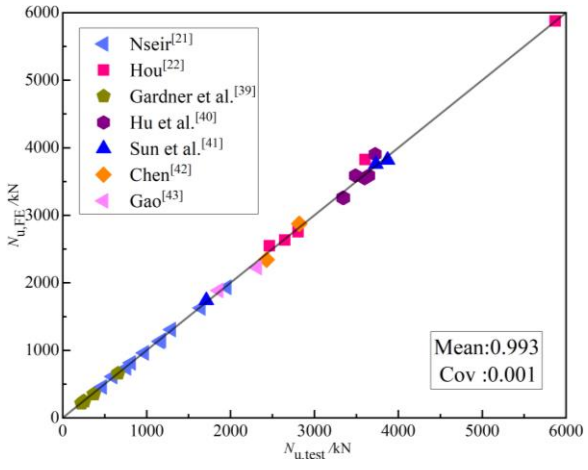

Fig. 8 Comparison results of ultimate capacities from tests and FE models

2.3. Settings of parametric studies

In order to explore the influences of the axial force ratio (n) and the width-to-thickness ratios of the flange (r_f) and web (r_w) on the ultimate capacity of the cold-formed SHS and RHS members, the parameters of specimens with different combinations of r_f, r_w, and n were analyzed in this paper. The definitions of the parameters are shown in Table 2.

Table 2
Definitions of parameters

Parameter	r_f	r_w	α	n
Definition	$r_f = \frac{b}{t\varepsilon_k}$	$r_w = \frac{h}{t\varepsilon_k}$	$\alpha = \frac{h}{b}$	$n = \frac{N}{N_y}$

Note: $\varepsilon_k = \sqrt{f_y/235}$, is the steel grade correction factor. $N_y = Af_{yf}$, indicates the yield axial load.

The settings of parametric studies are tabulated in Table 3. H = 300 mm, l = 3H = 900 mm, and r = 1.5t are consistent for all the parametric models. By

changing the section thickness t, flange width B and axial pressure force N, the combinations of r_f, r_w, and n are realized. Finally, 1336 FE models were obtained by parameter grouping, which include most of the cases that may occur in engineering and some cases that are impossible to occur but can be used as a comparison group in this study. In parametric analysis, the yield strength f_y and ultimate tensile strength f_u of the flat are 355 MPa and 442 MPa, respectively. For the corner, $f_y = 444$ MPa and $f_u = 523$ MPa. The axial compression member was named C-α-r_f (C indicates axial compression), and the member subjected to combined compression and bending was labeled BC-α-r_f (BC denotes combination of compression and bending).

Table 3
Parameter settings of sections

Parameter	Value
r_f	10 15 20 25 30 35 40 45 50 55 60 65 70 75 80 85 90 95 100 105
α	1 1.25 1.5 1.75 2 2.25 2.5 2.75 3
n	0 0.1 0.2 0.3 0.4 0.5 0.6 0.7 0.8 0.9

3. Results of FE modeling

3.1. Failure modes

3.1.1. Members under axial compression

Under axial compression, two distinct types of failure modes are commonly observed in the members: (1) the whole section of the member can reach the yield stress at the ultimate state, i.e., fully plastic failure (PF) and (2) local elastic-plastic buckling failure (EF).

Fig. 9 shows the failure process of typical members C-1-20, C-2.5-20, and C-2.5-40, including the Mises-stress nephogram at two critical states, the dimensionless load-displacement curve, and the mean stress development process at critical states, through which the development mechanism of local buckling and bearing capacities of the components with different failure modes are studied. The ultimate state refers to the moment when the member reaches ultimate capacity, and the final state refers to the moment when the bearing capacity drops to 80% of the ultimate capacity. The occurrence of local buckling is determined when mean stress (σ) reaches its maximum value.

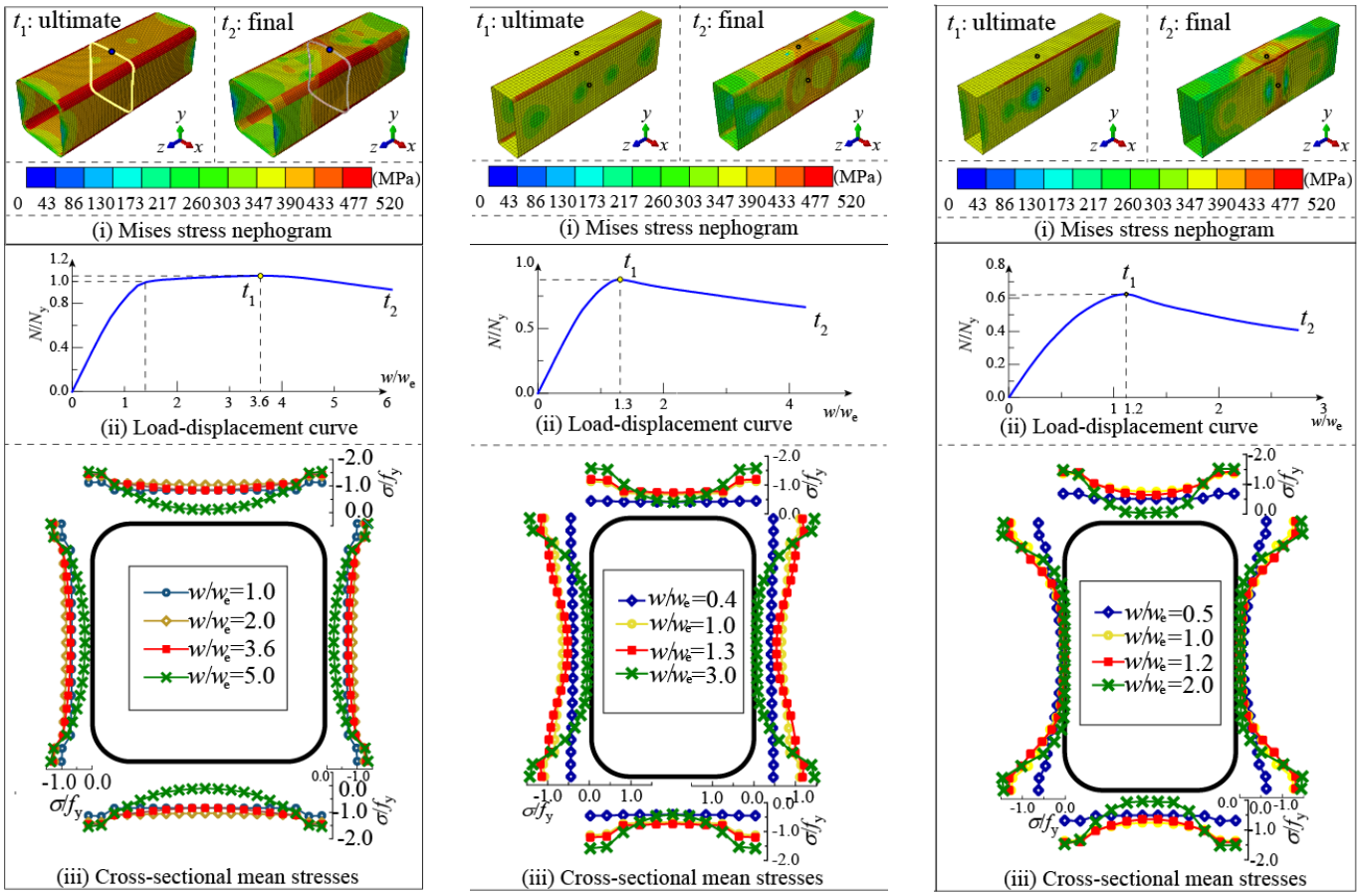

(a) C-1-20 (PF) (b) C-2.5-20 (EF) (c) C-2.5-40 (EF)

Fig. 9 Failure process of typical axial compression members

According to Fig. 9(a), C-1-20 occurs PF. The mean stress has reached the yield stress when w/w_e = 2.0, and the bearing capacity can further increase due to the cold-formed effect and strain hardening. When w/w_e = 3.6, slight plastic local buckling deformation is developed in the middle of plate, and the total stress of whole section reaches the maximum bearing capacity. At the final state, the section exhibits significant plastic deformation, but the decrease in bearing capacity is minimal, indicating that such sections possess excellent bearing capacity and ductility. According to Figs. 9(b) and 9(c), C-2.5-20 and C-2.5-40 experience EF, and the ultimate capacity of such members cannot reach the yield-bearing capacity. More specifically, at the ultimate state of C-2.5-20 (w/w_e = 1.3), the stress in the middle of the web begins to decrease, demonstrating that elastic buckling occurs on the webs. While for C-2.5-40, at the ultimate state (w/w_e = 1.2), both the flange and the web experience elastic local buckling. Compared with C-2.5-20, the web of C-2.5-40 undergoes severe local buckling at an earlier stage and has a more restricted critical buckling stress.

Therefore, the buckling degrees of plates in members subjected to axial compression is directly related to their width-to-thickness ratios. The higher the width-to-thickness ratio, the earlier local buckling occurs and the smaller critical local buckling stress. With the increase of the width-to-thickness ratios of the flange and web, the failure mode changes from PF to EF, and the bearing capacity and ductility also decrease.

3.1.2. Members under combined compression and bending

Despite the aforementioned failure modes for members under compression (PF and EF), members subjected to combined compression and bending exhibited elastic local buckling under axial pressure yet retained a degree of bending capacity due to post-buckling strength, leading to a compressive buckling failure (CB). Fig. 10 shows the failure mode process of typical components, namely, BC-1.25-40-0, BC-1.25-60-0.2, and BC-2.5-60-0.4, where M_{ec} and M_{pc} are the bending moment of edge yield and full-section plastic considering the axial pressure, respectively, and Δ_e is theoretical edge yield displacement. The failure mechanism and bearing performance of the members can be thoroughly examined through the analysis of bearing capacities of the components and changes of mean stress.

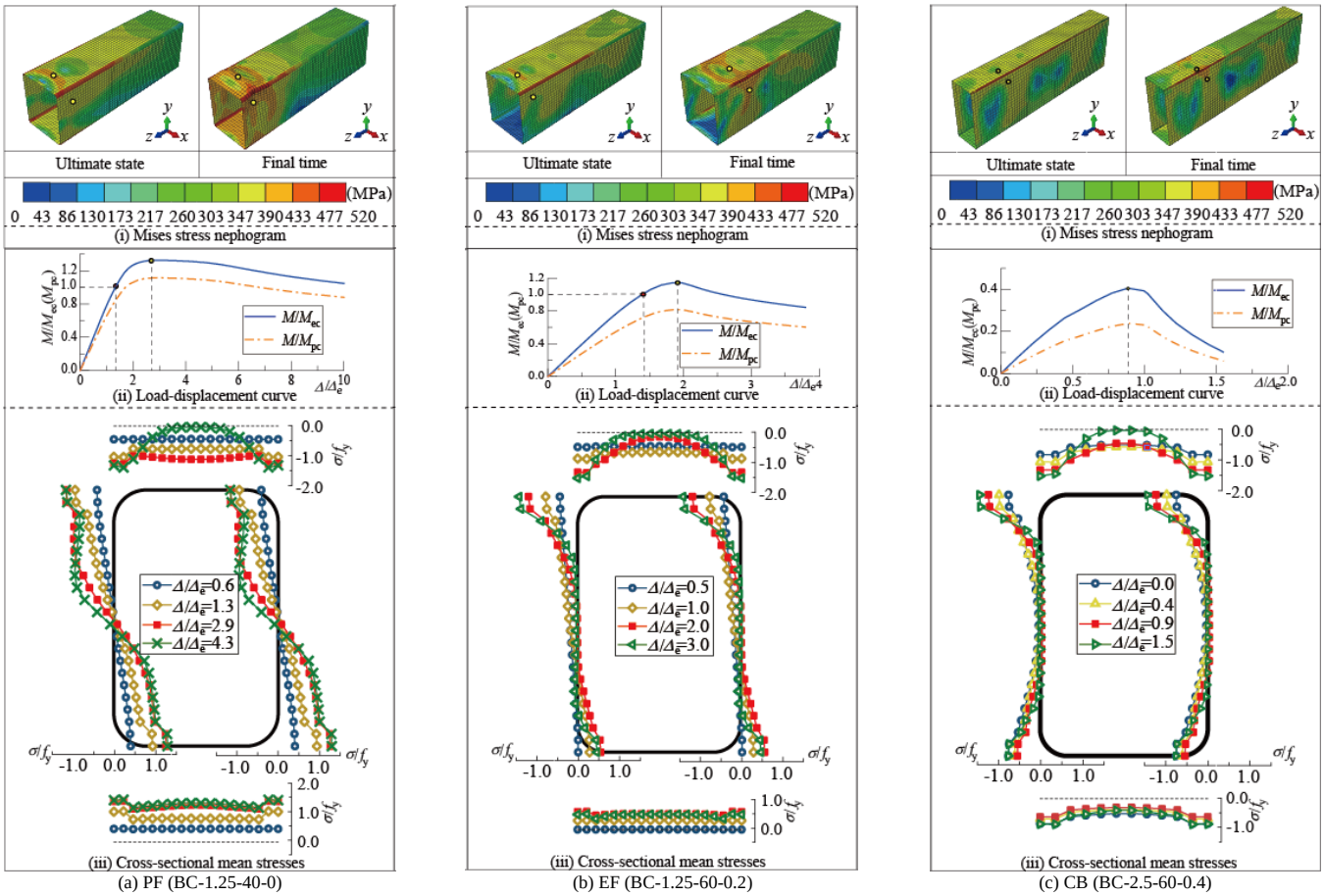

(a) PF (BC-1.25-40-0) (b) EF (BC-1.25-60-0.2) (c) CB (BC-2.5-60-0.4)

Fig. 10 Failure process of the typical members subjected to combined compression and bending

For BC-1.25-40-0, with relatively small flange width-to-thickness and aspect ratios, the whole section can develop plasticity at the ultimate state, allowing the ultimate capacity to reach M_{pc}. BC-1.25-60-0.2, with relatively large flange width-to-thickness and aspect ratios, the elastic local buckling of the compressive flange and web occurs before the ultimate state. Its ultimate capacity reaches M_{ec} but is less than M_{pc}. For BC-2.5-60-0.4, with large width-to-thickness ratios and axial force ratio, after the local elastic buckling occurs under axial pressure force, the local buckling of the compressive flange and web is further developed under the bending moment, while the local buckling of tensile flange tends to decrease. The ultimate capacity and ductility of this type of section are substantially limited, resulting in an ultimate capacity that is lower than M_{ec}.

Since the stress condition at the ultimate state is a direct reflection of the ultimate capacity of section, the stress at the ultimate state of typical section is extracted and compared to investigate the influence of various parameters on the ultimate capacity, as depicted in Fig. 11 and Fig. 12 according to the axial force ratio and plate width-to-thickness ratio, respectively. It is evident from Fig. 11 that the axial force ratio has little effect on the stress distribution of the compressive flange, but has significant effects on the web. Fig. 12(a) shows the stress distribution of the four members with the same flange width-to-thickness ratio and axial force ratio but different web width-to-thickness ratios, where it is observed that the specimens with larger web width than thickness have less web stress at the ultimate state. The interactive effect of plates, specifically, the smaller the width-to-thickness ratio of web, the greater constraining effect on the compressive flange with a similar r_f, leading to an increased stress in the compressive flange, is verified under this loading condition. Similarly, Fig. 12(b) shows that the stress of compressive flange decreases gradually at the ultimate state with an increase of the flange width-to-thickness ratio. It was shown that the smaller the flange width-to-thickness ratio, the more significant constraining effect on web, resulting in higher stress on the web. To sum up, the combination of n, r_f,and r_w exerts complex interactive effects on the failure modes and ultimate capacities of the members under any of the loading conditions discussed in the paper.

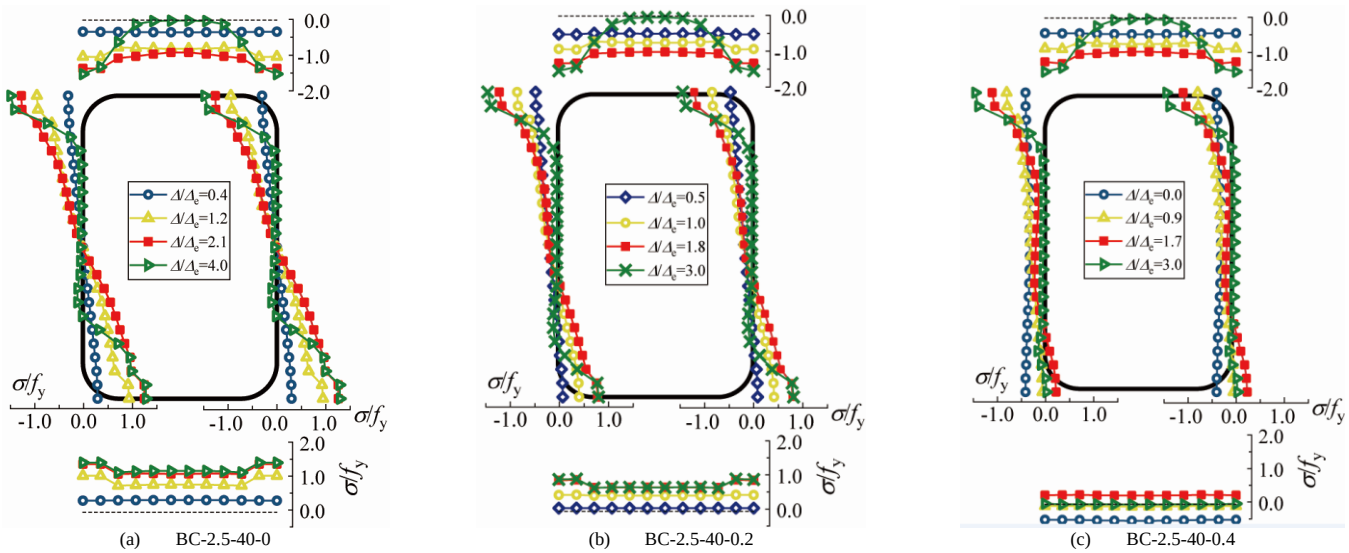

(a) BC-2.5-40-0 (b) BC-2.5-40-0.2 (c) BC-2.5-40-0.4

Fig. 11 Effects of the axial force ratios on stress distribution

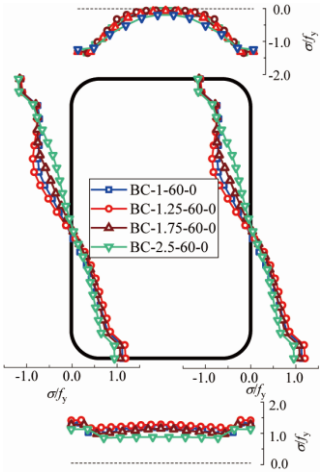

(a) Effects of r_f on stress distribution.

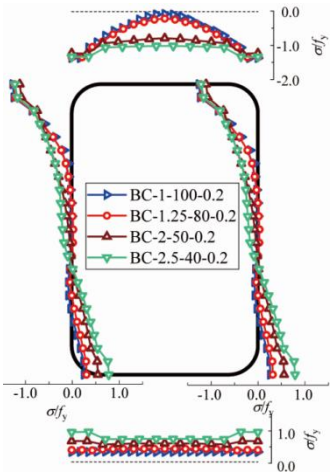

(b) Effects of r_w on stress distribution.

Fig. 12 Effects of width-to-thickness ratios of webs and flanges

3.2. Ultimate capacity

3.2.1. Ultimate compressive capacity

As depicted in Fig. 13(a), the dimensionless ultimate compressive capacity N_u/N_y represents the plastic development degree at the ultimate state. N_u/N_y decreases with an increase of width-to-thickness ratio of the flange as well as aspect ratio. The members with $N_u/N_y \geq 1$, as ranged with the orange area in Fig. 13(b), can achieve the full-section plasticity with certain strengthening. While for the members with $N_u/N_y<1$, as listed in the yellow area in Fig. 13(b), partially plastic effective sections can be reached at the ultimate state, providing a theoretical basis for the model of the axial compressive stress distribution of EPM.

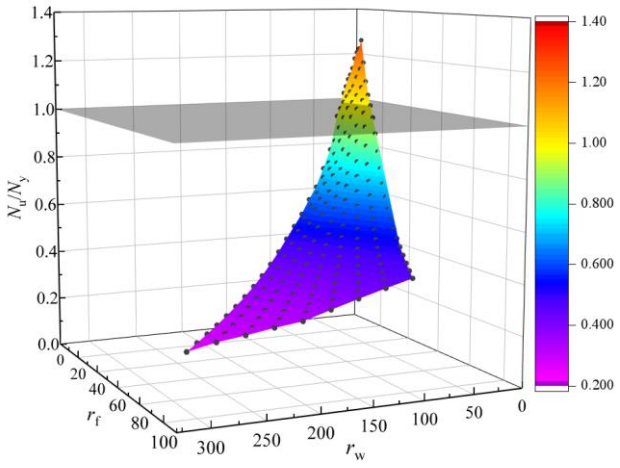

(a) Relationship between N_u/N_y, r_f,and r_w

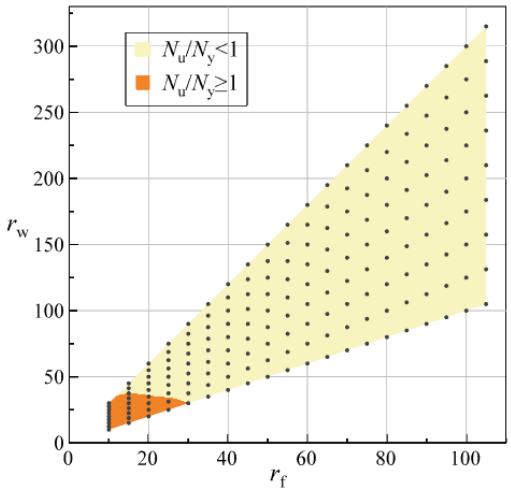

(b) Projection of the three-dimensional diagram

Fig. 13 The dimensionless ultimate compressive capacity

3.2.2. Ultimate bending capacity

As shown in Fig. 14, M_u/M_{pc} reflects the degree of the plasticity development of different sections at the ultimate state. M_u/M_{pc} decreases with an increase of r_f and r_w. When r_f is small, M_u/M_{pc} enlarges with an increase of n. When r_f and r_w are large, raising n enhances the local buckling of the plates, so M_u/M_{pc} declines with an increase of n.

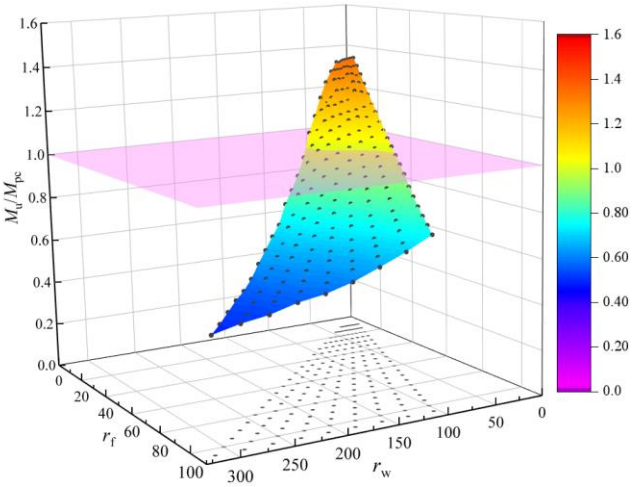

(a) Relationship between M_u/M_{pc}, r_f,and r_w (n = 0)

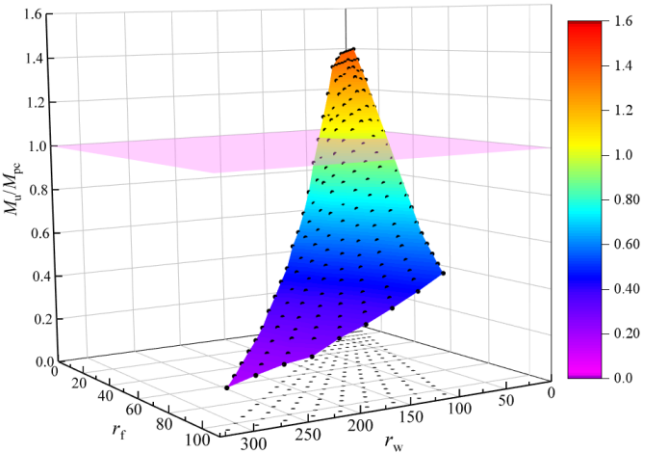

(b) Relationship between M_u/M_{pc}, r_f,and r_w (n = 0.2)

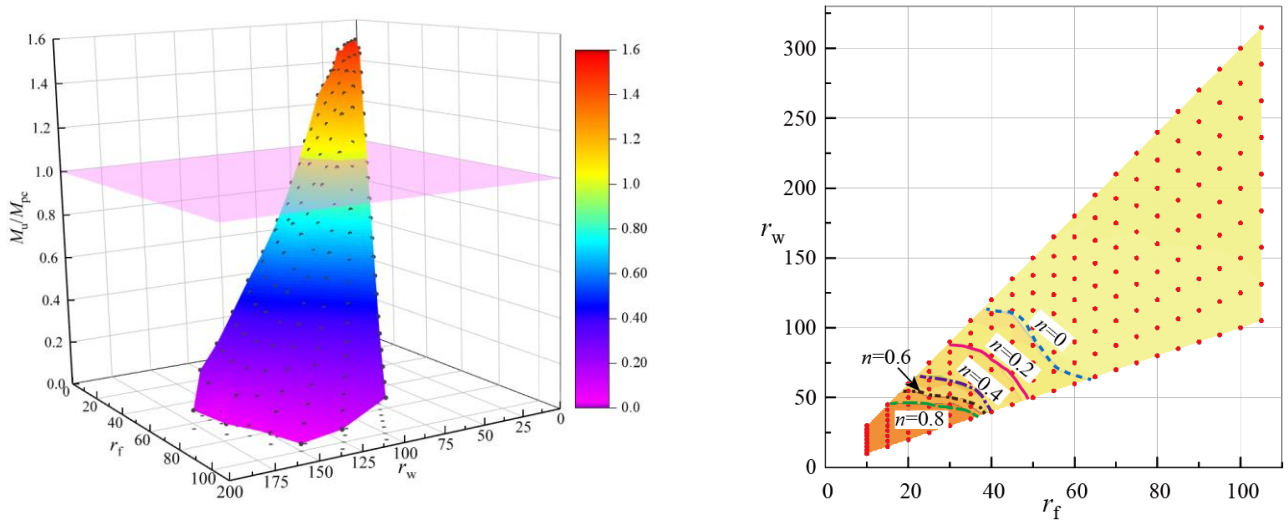

(c) Relationship between M_u/M_{pc}, r_f,and r_w (n = 0.4)

(d) Critical width-to-thickness ratio assembly curve

Fig. 14 Dimensionless ultimate bending capacity

Projecting the assembly curve of $M_u/M_{pc} = 1$ in Figs. 14(a)–(c) onto the *x*-*y* plane, as shown in Fig. 14(d), shows that the critical r_f and r_w continuously decrease with raising n. Below the critical curve, $M_u/M_{pc} > 1$, implying that the member can develop full-section plasticity and even play the role of strain hardening at the limit state. When the combination point is above the critical curve, $M_u/M_{pc} < 1$, indicating that the section can only develop partial plasticity at the limit state. This provides a theoretical basis for the stress distribution model of EPM under combined compression and bending.

4. Effective plastic width method

This section extends the application of EPM to calculate the ultimate capacities of cold-formed SHS and RHS members applicable to members within $r_f \leq 105$, $\alpha = 1-3$, and n = 0–0.9.

4.1. Ultimate compressive capacity

Due to different r_f and r_w values, the buckling degrees of the plates differ at the ultimate state. Thus, different stress distribution models are provided by distinguishing the fully and partially effective sections, and the formulas for calculating the ultimate compressive capacity are proposed using the effective plastic width and stress enhancement coefficient in this section.

4.1.1. Critical width-to-thickness ratio

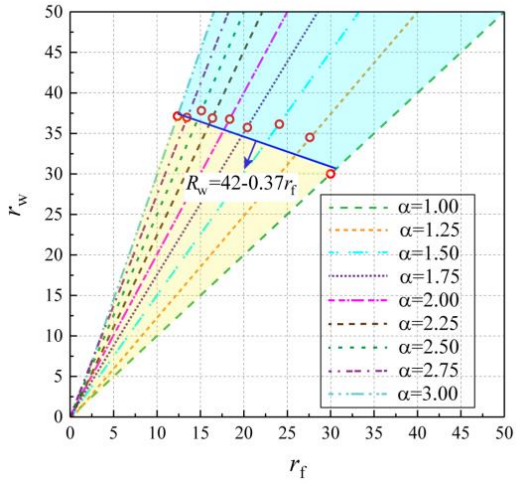

Fig. 15 The relationship between r_f and r_w when $N_u/N_y = 1$

In order to distinguish the fully effective sections from the partially effective sections, the limit curve in terms of r_f and r_w are extracted when $N_u/N_y = 1$ with different aspect ratios in the red dots, as shown in Fig. 15. and as expressed in Eq. (1):

$$R_w = 42 - 0.37 r_f \tag{1}$$

where R_w is the critical web width-to-thickness ratio of the cold-formed SHS and RHS members under axial load. When $r_w \leq R_w$, as the combination point is located in the yellow area in Fig. 15, the entire section is effective, and when $r_w > R_w$, the section is partially effective.

4.1.2. Stress distribution model of partially effective section

The stress in the middle area of a buckled plate at the ultimate state is close to zero, which can be regarded as the failure zone. Due to the support effect of adjacent flanges and webs, the mean stresses in and near the corner areas are maintained close to the yield stress, which can be regarded as the effective zones. The assumption is that the effective section and its stress distribution at the ultimate state are depicted in Fig. 16. Based on the stress distribution form, Eqs. (2)–(6) express the formulas for calculating the ultimate compressive capacity N_u.

$$N_u = 2N_f + 2N_w + 4N_c = 2b_e \cdot tf_y + 2h_e \cdot tf_y + 4l_c tf_y \tag{2}$$

$$b_e = \rho_{fc} \cdot b \tag{3}$$

$$h_e = \rho_{wc} \cdot h \tag{4}$$

$$\rho_{fc} = 13.5 r_f^{-0.75} \leq 1 \tag{5}$$

$$\rho_{wc} = k_w 13.5 r_w^{-0.75} \leq 1 \tag{6}$$

where N_f, N_w, and N_c are the bearing capacity of a single flange, web, and corner, respectively; h_e and b_e are the effective width of the plates, respectively; l_c indicates the centerline length of a corner; ρ_{fc} and ρ_{wc} represents the effective width coefficient of flange and web, respectively; k_w denotes the plate correlation interaction coefficient that considering the beneficial restraining effect of flange on the web and is expressed by $k_w = 0.95 + 0.05\alpha$.

4.1.3. Stress distribution model of fully effective section

For the fully effective sections, it is assumed that the stress on section σ_c is higher than yield strength to consider the favorable effect of strain hardening and the cold-formed effect. The stress distribution of the fully effective section is shown in Fig. 16(c), and its calculation formulas are expressed in Eqs. (7)–(8).

$$N_u = A\sigma_c = A \cdot \eta_c f_y \tag{7}$$

$$\eta_c = 1.35 - 0.003 r_f - 0.008 r_w \geq 1 \tag{8}$$

where η_c represents the stress enhancement coefficient under axial compression.

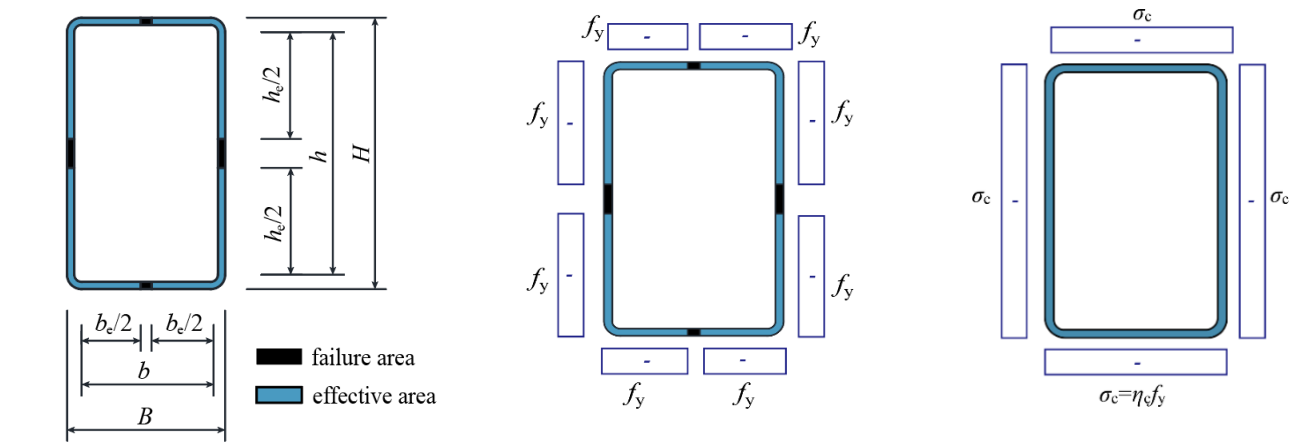

(a) The definition of the effective section (b) The stress distribution of the partially effective section (c) The stress distribution of the fully effective section

Fig. 16 The stress distribution models of the sections under axial compression

4.1.4. Evaluation of stress distribution models

In order to evaluate the calculation model of EMP under axial compression, the actual stress distribution of the typical model at the ultimate state is compared with the stress distribution model of EPM, as shown in Fig. 17, where the dotted red line and the dotted green line represent the stress distribution obtained from FEM and EPM, respectively. The axial compressive stress distribution model of EPM can effectively reflect the trend of the actual stress distribution and can consider the effects of strain hardening and plate buckling.

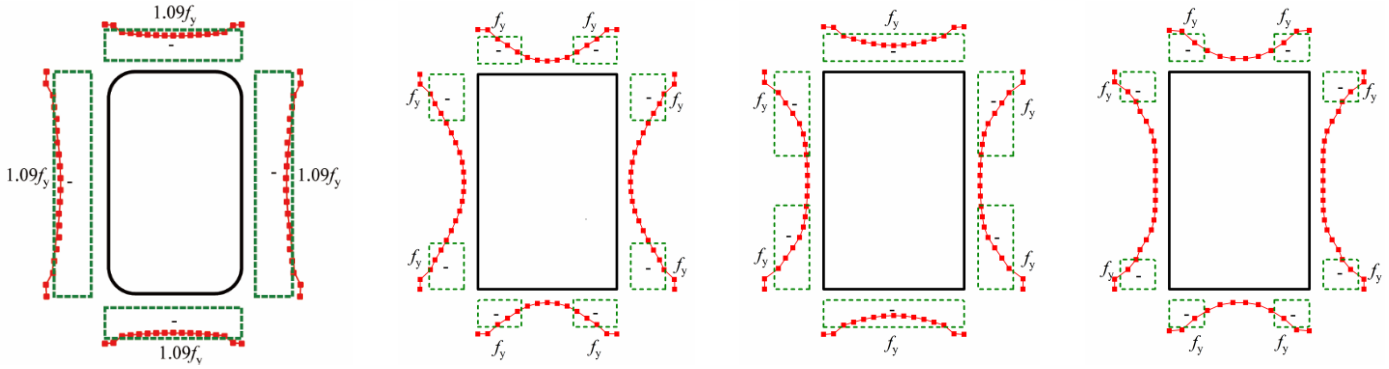

(a) C-1.25-20 (b) C-1.75-60 (c) C-2.5-20 (d) C-2.5-80

Fig. 17 Comparing the model of EPM with the FE results under axial compression

4.2. Ultimate bending capacity

In this section, two stress distribution modes under combined compression and bending are analyzed in detail, and the calculation formulas for calculating the ultimate bending capacity are proposed.

4.2.1. Stress distribution model of partially effective section

When the cold-formed SHS and RHS members under combined compression and bending reach ultimate state, different buckling forms and different development degrees will be generated under different combinations of r_f, r_w, and n. It is assumed that the normal stress generated by axial pressure is concentrated at the center of the webs, and with the axial pressure increases, this normal stress gradually extends to the flanges. In order to simplify the calculation, the failure zone of the web is assumed evenly distributed on both sides about the x-axis, and the stress σ_{bc} is used to consider the favorable effect of strain hardening and cold-formed effect. Based on above assumptions, the stress distribution mode of partially effective section is divided into four cases according to the different effective sections and axial force ratios, as shown in Fig. 18. The four stress distribution models proposed take into account various combination situations of axial compression and bending moment.

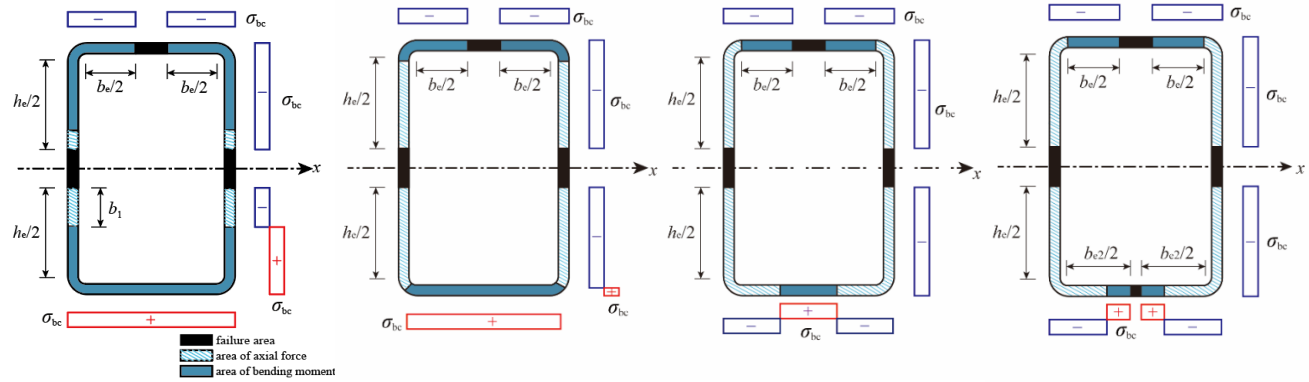

(a) Case 1 (b) Case 2 (c) Case 3 (d) Case 4

Fig. 18 Stress distribution models of partially effective sections under compression and bending

(1) Case 1

When axial force levels are relatively low, compressive stress is only distributed on the web, i.e., $b_1 < h_e/2$, where b_1 is the width of the compressive stress due to the axial pressure distributed on the lower side of the *x*-axis, and can be obtained according to the balance of the axial forces. In this scenario, the compressive plates experience local buckling with the settlement of the failure zone, while the tensile flange remains fully effective, as depicted in Fig. 18(a). The formula for calculating the ultimate bending capacity M_u can be obtained by taking the moment of the stress on the section to the *x*-axis, as expressed in Eqs. (9)–(13).

$$M_u = M_c + M_f + M_w \tag{9}$$

$$M_c = \left(\frac{4(R^3 - r^3)}{3} + \frac{\pi h(R^2 - r^2)}{2}\right)\sigma_{bc} \tag{10}$$

$$M_f = (b_e + b)t\sigma_{bc} \cdot \frac{H}{2} \tag{11}$$

$$M_w = 4\left(\frac{h_e}{2} - b_1\right)t\sigma_{bc} \cdot \left(\frac{h}{2} - \frac{h_e}{4} + \frac{b_1}{2}\right) \tag{12}$$

$$b_1 = \frac{(nl_1 + b - b_e)f_y}{4\sigma_{bc}} \tag{13}$$

where M_f, M_w, and M_c are the bending moment components of the flange, web, and corner, respectively; l_1 is the centerline length of the entire section.

(2) Case 2

As axial pressure increases, compressive stress extends to the corner zone but not reaches the tensile flange, that is, $h_e/2 < b_1 < h_e/2 + l_c$, as presented in Fig. 18(b). The compressive plates experience partially effective due to local buckling, and the tensile flange is fully effective. Compared with Case 1, the web in Case 2 is all compressive, and no bending moment is generated by the webs. Thus, M_c is reduced to M_c' under the influence of extended compressive stress.

$$M_u = M_c' + M_f \tag{14}$$

$$M_c' = M_c - \left(\frac{8(R^3 - r^3)\sin^2(\theta/2)}{3} + \theta h(R^2 - r^2)\right)\sigma_{bc} \tag{15}$$

where θ is the radian value of the compressive stress penetrating the corner and is expressed in $\theta = \frac{b_1 - h_e/2}{(R+r)/2}$.

(3) Case 3

As the axial pressure increases, compressive stress is distributed across the web, corner, and the tensile flange which is $b_1 > h_e/2 + l_c$, as depicted in Fig. 18(c). Neither the web nor the corner generates the bending moment member, and the bending moment is generated by the stress in the top and bottom flanges. Substituting the formula for calculating b_1 into Eq. (17) yields Eq. (18).

$$M_u = M_f' \tag{16}$$

$$M_f' = (b_e + b + 2h_e + 4l_c - 4b_1)t\sigma_{bc} \cdot \frac{H}{2} \tag{17}$$

$$M_u = (2b_e + 2h_e + 4l_c - nl_1)t\sigma_{bc} \cdot \frac{H}{2} \tag{18}$$

(4) Case 4

As axial pressure approaches the ultimate compressive capacity, local buckling would occur at all the plates subjected to axial pressure and bending moment, and the failure zone appears, as depicted in Fig. 18(d), where the effective width of tensile flange is b_{e2}. No bending moment member is generated by the webs and the corner zones, thus $M_u = M_f'$. Eqs. (20)–(22) express the calculation process, where M_{f1} and M_{f2} indicate the bending moment components of tensile flange and compressive flange to *x*-axis, respectively. Substituting Eq. (19), the calculation formula for b_1, into Eq. (22) yields the final formula for calculating M_u. The final formula is the same as Eq. (18), which indicates that the calculation of the ultimate bending capacity in Case 3 and 4 can be considered in the same case.

$$b_1 = \frac{(nl_1 + b_{e2} - b_e)f_y}{4\sigma_{bc}} \tag{19}$$

$$(b_1 - h_e/2 - l_c))t\sigma_{bc} \cdot \frac{H}{2} = (b_{e2} - 2b_1 + h_e + 2l_c)t\sigma_{bc} \cdot \frac{H}{2} \tag{20}$$

$$M_{f2} = (b_e - 2(b_1 - h_e/2 - l_c))t\sigma_{bc} \cdot \frac{H}{2} = (b_e - 2b_1 + h_e + 2l_c)t\sigma_{bc} \cdot \frac{H}{2} \tag{21}$$

$$M_f' = M_{f1} + M_{f2} = (b_e + b_{e2} + 2h_e + 4l_c - 4b_1)t\sigma_{bc} \cdot \frac{H}{2} \tag{22}$$

4.2.2. Stress distribution model of fully effective section

When the width-to-thickness ratio of the members is small, the section can develop full plasticity at the ultimate state. According to different axial force levels, the stress distribution mode of the fully effective section can be divided into three cases, as shown in Fig. 19.

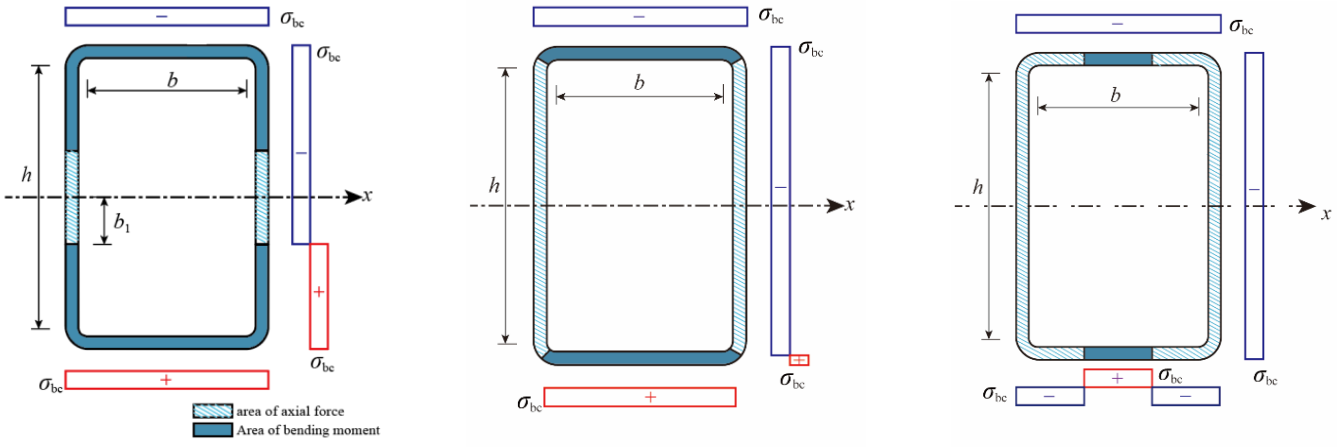

(a) Case 1 (b) Case 2 (c) Case 3

Fig. 19 The stress distribution models of the fully effective sections under compression and bending

For the three cases, the ultimate bending capacity is still calculated by the formula of situations in Figs. 18(a)–(c), by replacing b and h into b_e and h_e into the corresponding formulas respectively. The stress distribution mode of the fully effective section can consider the strengthening effect of the material and the cold-formed effect of the corner by taking the enhancement of the section stress into account. The stress distribution model of case 3 can regress to the stress distribution of the fully effective section in Fig. 16(c), indicating that EPM stress distribution model of the fully effective section can completely return the situation of combine compression and bending to the axial compression situation.

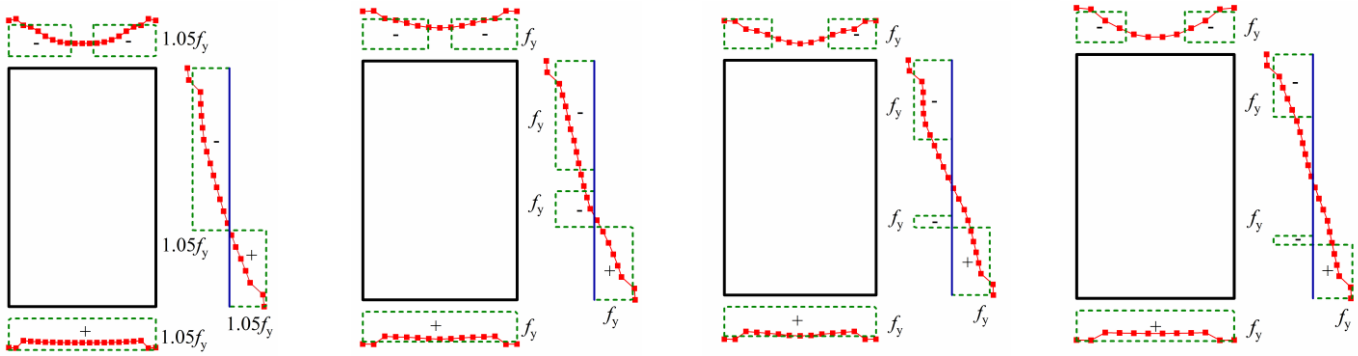

(a) BC-1-40-0.2 (b) BC-1.75-40-0.2 (c) BC-1.75-60-0 (d) BC-2.5-60-0

Fig. 20 Comparing the model of EPM and the FE results under compression and bending

4.2.4. Effective plastic width and stress enhancement coefficient

(1) Effective plastic width

The effective plastic width is a critical parameter of EPM, which not only reflects the reduction of the bearing capacity caused by local buckling and interactive effect of plates, but also represents the balance of the effective section under the simplified plastic stress distribution. It can be obtained by observing parametric analysis results and summarizing the stress development law.

The compressive flange is fully compressive at different axial force ratios. Therefore, it can be assumed that the effective width (b_e) of the compressive flange equals that of the plate under axial pressure, as expressed in Eq. (23). The calculation formula for fitting the effective width (h_e) of the web is provided in Eq. (24), where ρ_{wb} represents the effective width coefficient of the web under combined compression and bending (Eq. 25). When the axial force ratio reaches its maximum allowable value for the section, the member is infinitely close to the axial compression state, and n can be obtained using Eq. (26). By substituting n into Eq. (25), $\rho_{wb} = \rho_{wc}$ can be obtained, and the stress distribution and effective width of the section are similar to that of the axial compression state.

$$b_e = \rho_{fc} \cdot b \tag{23}$$

$$h_e = \rho_{wb} \cdot h \tag{24}$$

$$\rho_{wb} = \rho_{wc} + [1 - (\frac{n(\alpha+1)}{\rho_{fc}(k_w \alpha^{0.25}+1)})^3] \cdot (\frac{20}{r_w} + \frac{0.1}{\alpha}) \le 1 \tag{25}$$

$$n = \frac{N_u}{Af_y} = \frac{2(\rho_{fc} b + \rho_{wc} h) t f_y + N_c}{Af_y} \approx \frac{\rho_{fc} b + \rho_{wc} h}{b+h} = \frac{\rho_{fc}(k_w \alpha^{0.25}+1)}{\alpha+1} \tag{26}$$

(2) Stress enhancement coefficient

When both the flange and the web are partially effective, the increase of the section stress is not considered, and the section stress equals f_y, i.e., $\sigma_{bc} = f_y$. For members with the fully effective section and effective web, the favorable cold-formed effect and strain hardening on the ultimate bending capacity can be considered by the stress enhancement coefficient (η_{bc}). Eqs. (27) and (28) express the formulas for calculating η_{bc} and σ_{bc} respectively. When the axial force ratio of the member with the fully effective section reaches the maximum axial force ratio it can bear, that is, $n = \eta_{bc}$ and $\eta_{bc} = \eta_c$, the stress distribution of the section equals that of the fully effective section under axial compression.

$$\eta_{bc} = \eta_c + (1 - \frac{n}{\eta_c}) \cdot \frac{\alpha(100 - 0.5 r_w)}{1200} \ge 1 \tag{27}$$

$$\eta_{bc} = \eta_c + (1 - \frac{n}{\eta_c}) \cdot \frac{\alpha(100 - 0.5 r_w)}{1200} \ge 1 \tag{28}$$

5. Evaluation of calculation methods of EPM and specifications

This section summarizes the current design methods for calculating bearing capacities of members in EC3 and GB50018, and the proposed EPM is compared with the specifications to evaluate its feasibility.

5.1. Evaluation of existing specifications

5.1.1. EC3

The European Code, i.e., EC3, calculates the section bearing capacity based on section classification according to the width-to-thickness ratios of plates, adopting different design criteria. The sections are categorized into classes according to the influence degree of local buckling on bearing capacity. However, EC3 has following shortcomings when calculating the ultimate capacity of different sections:

- The ultimate capacities of classes 1 and 2 sections are partially conservative without considering strain hardening.
- The bearing capacities of sections of classes 2 and 3 are discontinuous because the partial plasticity of the sections is not considered.
- The calculation process of the section of class 4 is complex, which is not conducive to the actual operation.
- EC3 is conservative for compact sections but unsafe for slender ones, and EC3 section classification cannot be directly applied to cold-formed steel members.
- EC3 follows the principle of single plate when classifying sections, assuming that the plate is supported on four sides without considering the interaction between the flanges and webs, and the bearing capacity calculation is not accurate enough.

5.1.2. GB50018

Code GB50018 is applicable for cold-formed steel members with a plate thickness ranging from 2 to 6 mm. When calculating the ultimate capacity of cold-formed SHS and RHS members in code GB50018, the plate failure caused by local buckling can be well-considered for thin members. However, the following shortcomings may exist:

- The application scope of the code on thickness is limited. For cold-formed SHS and RHS members beyond the scope, its application is still controversial.

- GB50018 does not consider the development of section plasticity and dramatically underestimates the ultimate capacity of cold-formed SHS and RHS members with small width-to-thickness ratios, so the bearing capacity of cold-formed steel members cannot be fully utilized.
- When calculating the effective width of compression plate, the changes in interactive effects of plates after buckling are ignored, so the calculation of the bearing capacity is conservative.

5.2. Comparison of calculation methods

To assess the accuracy of GB50018, EC3, and EPM, their calculation results of these three methods are compared with parametric analysis results.

5.2.1. Comparison of ultimate compressive capacity

The ultimate compressive capacities of the members determined by GB50018 ($N_{u,GB50018}$), EC3 ($N_{u,EC3}$), EPM ($N_{u,EPM}$), and the FE model ($N_{u,FEM}$) are compared in dimensionless terms. The results of different aspect ratios are shown in Fig. 21. The results of EPM, EC3, and GB50018 are relatively close to those of the FE model, and GB50018 tends to be the most conservative method. When the aspect ratio is small, the ultimate compressive capacity predicted by EC3 is unsafe, and it is close to the FE model results at aspect ratios higher than 2.25. Both specifications fail to consider the strain hardening at small width-to-thickness ratios, leading to conservative calculation results. Nevertheless, EPM aligns most closely with the results from FE calculations.

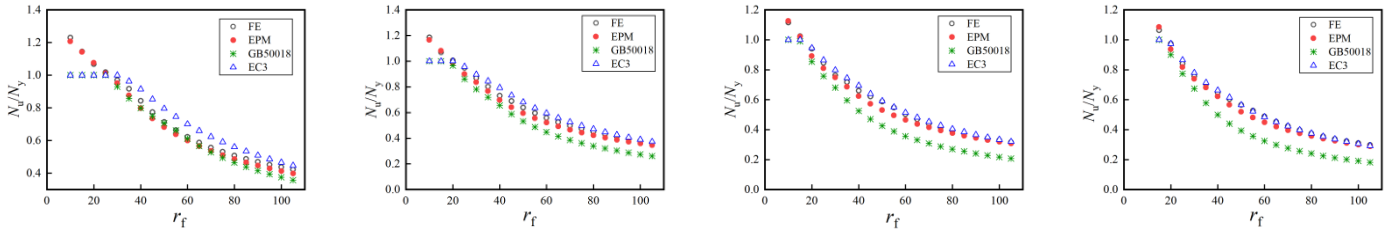

(a) α = 1.25 (b) α = 1.75 (c) α = 2.25 (d) α = 2.75

Fig. 21 Comparison of the ultimate compressive capacity of the members

The calculations and simulation results are plotted in Fig. 22. Generally, more than half of the results of GB50018 fall outside the -10% range of the diagonal line, indicating that most of the results are conservative. The EC3 calculation method is close to the FE results, and most points fall within the +10% range of the diagonal line. The proposed EPM is very close to the diagonal line, and its calculations are accurate. The above conclusions can also be further confirmed by comparing the results of average value and variance in Table 4.

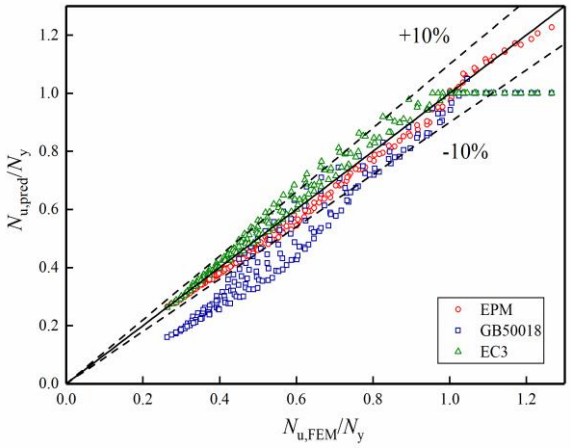

Fig. 22 Evaluation of the ultimate compressive capacity of the members calculated using three methods

Table 4
Comparison of the ultimate compressive capacity calculated using three methods with respect to the FE result

	$N_{u,EPM}$ / $N_{u,FEM}$	$N_{u,GB50018}$ / $N_{u,FEM}$	$N_{u,EC3}$ / $N_{u,FEM}$
Average value	0.960	0.813	1.029
Variance	0.001	0.016	0.004

5.2.2. Comparison of ultimate bending capacity

The ultimate bending capacities of the members, as determined by GB50018 ($M_{u,GB50018}$), EC3 ($M_{u,EC3}$), EPM ($M_{u,EPM}$), and the FE model ($M_{u,FEM}$) are presented in a dimensionless form relative to M_{pc} and are illustrated in Fig. 23, categorized according to different axial force ratios. EPM and FE results are relatively close, and most EPM points fall below the FE results, showing that its calculations are slightly conservative.

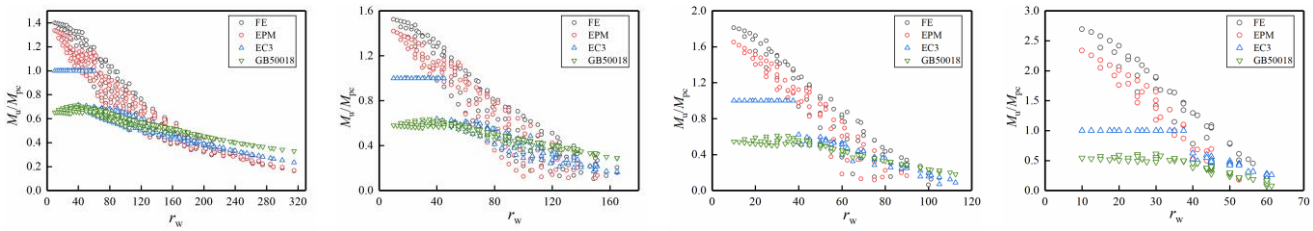

(a) n = 0.2 (b) n = 0.4 (c) n = 0.6 (d) n = 0.8

Fig. 23 Comparison of the ultimate bending capacity of the members calculated using EPM, GB50018, and EC3

The calculations and simulation results are plotted in Fig. 24 to directly examine the deviation degree of the three calculation methods from the FE model. Table 5 tabulates the average value and variance. According to Fig. 24, the trend of the calculation results of GB50018 deviates from that of the FE. Further, the average value of the ratio is the smallest, and the degree of dispersion is large. EC3 can predict the bearing capacity of members with thin

plates accurately. Additionally, with an increase of *n*, the overall prediction is conservative, and the ratio average is small. The trend of the change in the overall prediction of EPM is consistent with that of the FE results. When *n* is small, it is very close to the FE data, and the prediction is slightly conservative at large *n* values. However, compared with the calculation results of GB50018 and EC3, EPM can provide more accurate results. The average value of the ultimate bending moment of members calculated by EPM with respect to that calculated by the FE model, is close to 1.0 with an essentially small dispersion.

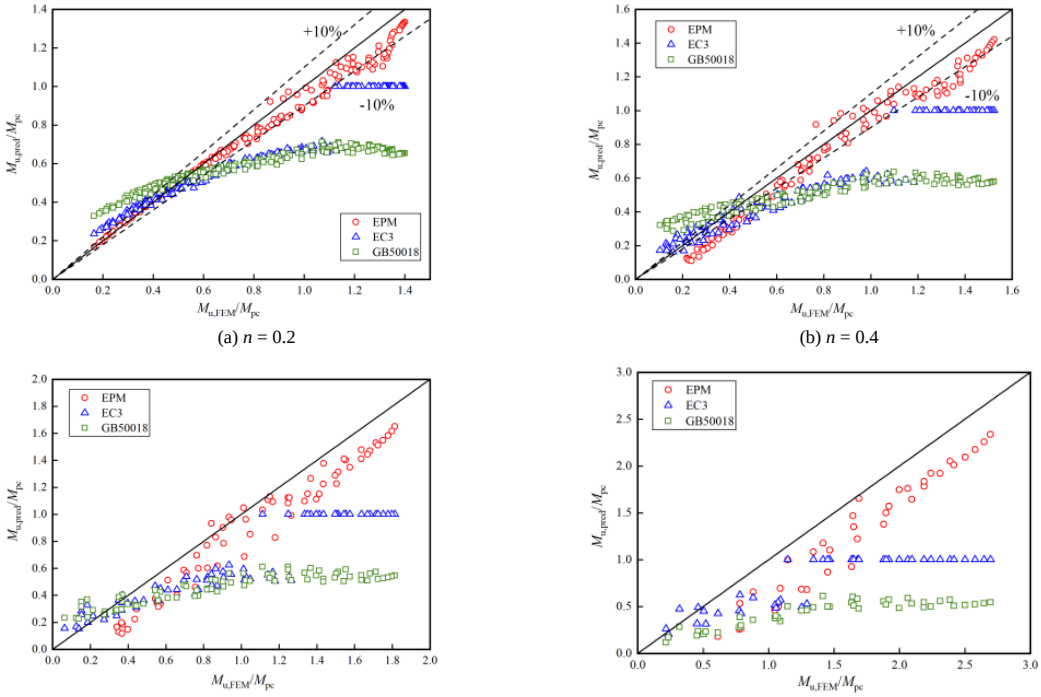

(a) n = 0.2 (b) n = 0.4

(c) n = 0.6 (d) n = 0.8

Fig. 24 Evaluation of the ultimate bending moments calculated using EPM, GB50018, and EC3

Table 5
Comparison of ultimate capacities calculated using three methods with the FE data

		$M_{u,EPM}$ / $M_{u,FEM}$	$M_{u,GB50018}$ / $M_{u,FEM}$	$M_{u,EC3}$ / $M_{u,FEM}$
n = 0.2	Average value	0.966	0.879	0.878
	Variance	0.003	0.107	0.031
n = 0.4	Average value	0.860	0.756	0.768
	Variance	0.018	0.110	0.025
n = 0.6	Average value	0.801	0.527	0.663
	Variance	0.029	0.035	0.018
n = 0.8	Average value	0.719	0.311	0.540
	Variance	0.032	0.016	0.006

EPM calculates the ultimate capacity of members based on the actual stress distribution across the section at the limit state, accurately reflecting the real stress conditions of the members. At its core, the method equates the ultimate capacity with the bearing capacity of the effective plastic section. EPM effectively accounts for strain hardening and cold-formed effects of classes 1 and 2 sections, allows for the partial plastic development in class 3 sections, and accommodates the local buckling in class 4 sections by considering the effective plastic width b_e and the stress enhancement coefficient η_{bc}. This approach overcomes the discontinuities often found in ultimate capacity predictions and transcends the limitations imposed by section classification on ultimate capacity. It also considers the influence of the interactive effect of plates. With its straightforward concept and simple operation, EPM avoids complex iterations, enabling precise calculations of the ultimate capacity for cold-formed SHS and RHS steel members without the need for intricate procedures.

6. Conclusions

In this study, a comprehensive parametric study was conducted on cold-formed SHS and RHS steel pipes with various combinations of flange and web width-to-thickness ratios as well as axial force ratios. The research investigated and analyzed the failure modes and bearing capabilities of these cold-formed members under compression and combined compression and bending. Based on the stress distribution of section at the limit state, EPM was introduced for calculating the ultimate capacity of cold-formed SHS and RHS members. The prediction accuracy of EPM was assessed alongside current standards, using FE simulations and experimental data. The key conclusions of this study are as follows:

- Cold-formed SHS and RHS members exhibit varying degrees of local buckling at the limit state, influenced by width-to-thickness ratios and axial force ratios. Buckling severity dictates the failure modes, which for axial compression, range from the fully plastic failure to local elastic-plastic buckling failure. Under combined compression and bending, failure modes include fully plastic failure, local elastic-plastic buckling failure, and compressive buckling failure.
- Stress distribution at the limit state of member can be categorized into fully effective section and partially effective section, with corresponding stress distribution models that more accurately reflect actual stress trends and account for strain hardening and plate buckling effects.
- Depending on the axial force ratios, partially effective stress distribution models are classified into four cases, whereas fully effective section models are split into three. EPM stress distribution model, especially under high axial force ratios, effectively bridges the gap between combined compression and bending to axial compression scenarios, allowing the use of identical calculation formulas, demonstrating significant theoretical value.
- Comparative analysis with FE results and experimental data reveals that the ultimate capacity predictions by the GB50018 standard are conservative. In contrast, the compressive capacity predictions by EC3 are slightly unsafe. The bending resistance predictions by EC3 are relatively precise. However, the ultimate resistance predictions by EPM are notably more accurate.
- EPM, based on the actual stress distribution at the limit state, closely reflects the real stress conditions in members, offering accurate predictions of the ultimate capacities of cold-formed SHS and RHS members. By considering the effective plastic width and the stress enhancement coefficient, the method comprehensively addresses strain hardening, cold-formed effect, and interactive effects of plates, avoiding prediction discontinuities and making more precise calculations.

Acknowledgments

The research received support from the General Program of the National Natural Science Foundation of China (Grant No. 51978437), the Excellent Youth Cultivation Program of Shanxi Basic Research Plan (Grant No. 202103021222007), and China Postdoctoral Science Foundation Project (Grant No. 2021M692862).

References

[1] Chen, Y.Y., Wang, W. and Zhou, F. Steel tubular structures: configuration innovation and performance improvement driven by new requirements. Journal of Building Structures, 2019:1-20.

[2] Hou, G., Tong, L.W., Chen, Y.Y. and Li, Z.G. Testing and analysis model for material property of non-thin-walled cold-formed square hollow sections. Engineering Mechanics, 2013. 30(2):372-378,426.

[3] Tong, L.W., Huo, T. and Hou, G. Research on design formula for yield strength of cold-formed rectangular steel tubes with medium-thick wall. Journal of Building Structures, 2018. 39(12):81-90.

[4] Guo, Y.J., Zhu, A.Z., Pi, Y.L. and Tin-Loi, F. Experimental study on compressive strengths of thick-walled cold-formed sections. Journal of Constructional Steel Research, 2007. 63(5): 718-723. https://doi.org/10.1016/j.jcsr.2006.08.008

[5] Wang, W., Fang, C., Qin, X., Chen, Y.Y. and Li, L. Performance of practical beam-to-SHS column connections against progressive collapse. Engineering Structures, 2016. 106(Jan.1): 332-347. https://doi.org/10.1016/j.engstruct.2015.10.040

[6] Wang, W., Fang, C., Chen, Y.Y. and Wang, M.X. Seismic performance of steel H-beam to SHS-column cast modular panel zone joints. Engineering Structures, 2016. 117: 145-160. https://doi.org/10.1016/j.engstruct.2016.03.006

[7] Fang, C., Zhou, F. and Luo, C.H. Cold-formed stainless steel RHSs/SHSs under combined compression and cyclic bending. Journal of Constructional Steel Research, 2018. 141: 9-22. https://doi.org/10.1016/j.jcsr.2017.11.001

[8] Zhou, F., Fang, C. and Chen, Y.S. Experimental and numerical studies on stainless steel tubular members under axial cyclic loading. Engineering Structures, 2018. 171: 72-85. https://doi.org/10.1016/j.engstruct.2018.05.093

[9] Fang, C., Wang, F.C., Wang, C.Y. and Zheng, Y. Cyclic behavior of oval hollow section (OHS) beam-columns. Thin-Walled Structures, 2021. 161: 1-14. https://doi.org/10.1016/j.tws.2020.107430

[10] CSADI. Technical code of cold-formed thin-wall steel structures, in GB50018-2002. 2002, Wuhan.

[11] CEN (European Committee for Standardization). Eurocode 3: Design of steel structures–Part 1-1: General rules and rules for buildings, in EN 1993-1-1:2005. 2005, Brussels, Belgium.

[12] Wu, Y.G. and Zhang, Q.L. Study on post-buckling plate assembly effect of rectangular tube under uniform compression. Chinese Quarterly of Mechanics, 2006. 27(2): 286-294.

[13] Shen, H.X. Buckling coefficients taking into account constraint actions between plate elements of lipped channel struts. Steel Construction, 2006. 21(1): 62-64.

[14] Li, Y.Q., Li, G.W., Shen, Z.Y., Ma, Y.F. and Zhu, S.W. Design reliability analysis of cold-formed thick-walled-steel members under axial compression. Journal of Building Structures, 2015. 36(5): 8-17.

[15] Wen, D.H., Shen, Z.Y., LI, Y.Q. and Zhu, S.W. Experimental research on cold-formed thick-walled steel box stubs and comparison of results with related codes. Journal of Tongji University (Natural Science), 2016. 44(8): 1190-1198.

[16] Hu, S.D., Li, L.X. and Zhou, J.L. Strain hardening of thick-walled cold formed steel rectangular hollow section. Journal of Building Structures, 2011. 32(6): 76-81.

[17] Wang, J., Afshan, S., Schillo, N., Theofanous, M., Feldmann, M. and Gardner, L. Material properties and compressive local buckling response of high strength steel square and rectangular hollow sections. Engineering Structures, 2017. 130(JAN.1): 297-315. https://doi.org/10.1016/j.engstruct.2016.10.023

[18] Ma, J.L., Chan, T.M., and Young, B. Experimental investigation on stub-column behavior of cold-formed high-strength steel tubular sections. Journal of Structural Engineering, 2016. 142(5): 04015174. https://doi.org/10.1061/(ASCE)ST.1943-541X.0001456

[19] Ma, J.L., Chan, T.M., and Young, B. Design of cold-formed high-strength steel tubular stub columns. Journal of Structural Engineering, 2018. 144(6): 04018063. http://dx.doi.org/10.1061/(ASCE)ST.1943-541X.0002046

[20] Ma, J.L., Chan, T.M., and Young, B. Cold-formed high-strength steel rectangular and square hollow sections under combined compression and bending. Journal of Structural Engineering, 2019. 145(12): 04019154. https://doi.org/10.1061/(ASCE)ST.1943-541X.0002446

[21] Nseir, J. Development of a new design method for the cross-section capacity of steel hollow sections. 2015, Belgium: Université de Liège.

[22] Hou, G. Experimental research and numerical analysis on axial compression performance of cold-formed non-thin-walled square hollow sections. 2011, Tongji University: Shanghai.

[23] Yao, X.Y., Guo, Y.L., Liu, Z.Y. and Song, H. Experimental study and load-carrying capacity analysis of cold-formed thin-walled steel axially-compressed rectangular hollow steel columns. Architecture Technology, 2015. 46(09): 853-856.

[24] Yun, X., and Gardner, L. The continuous strength method for the design of cold-formed steel non-slender tubular cross-sections. Engineering Structures, 2018. 175: 549-564. https://doi.org/10.1016/j.engstruct.2018.08.070

[25] Deng, J.M. Research on the local buckling behavior of cold-formed thin-walled SHS and RHS based on CSM. 2018, Chang'an University.

[26] Ma, J.L., Chan, T.M., and Young, B. Cold-formed high strength steel tubular beam-columns. Engineering Structures, 2021. 230(1–3): 111618. https://doi.org/10.1016/j.engstruct.2020.111618

[27] Li, Y.Q., Shen, Z.Y., Wang, L., Wang, Y.M. and Xu, H.L. Analysis method for load-carrying capacity of 550MPa high-strength cold-formed thin-walled steel columns subjected to axial compression. Journal of Building Structures, 2006. 27(3): 18-25.

[28] Chen, S.F. and Hui, Y. Interaction of local buckling in cold-formed members and effective width of edge-stiffened elements. Journal of Xi'an University of Architecture & Technology, 1995. 27(1): 1-7.

[29] Chen, S.F. Plate interactive buckling and ultimate capacity of cold-formed sections. Progress in Steel Building Structures, 2002. 4(01): 3-6.

[30] Chen, Y.Y., Ma, Y., Zhao, J. and Tong, L.W. Tests on high frequency welded H-steel columns with slender elements and its evaluation of seismic resistance. Journal of Tongji University (Natural Science), 2006. 34(11): p. 1421-1426.

[31] Cheng, X. and Chen, Y.Y. Ultimate strength of H-sections under combined compression and uniaxial bending considering plate interaction[J]. Journal of Constructional Steel Research. 2018, 143: 196-207.

[32] Shi, X.P., Cheng, X., Wang, X.X. and Mansour, M. Ultimate behavior and design of cold-formed steel square hollow section members. International Journal of Steel Structures, 2022. 22(3): 767-790. https://doi.org/10.1007/s13296-022-00605-2

[33] CEN (European Committee for Standardization). Eurocode 3: Design of steel structures-Part 1-5:Plated structural elements, in EN 1993-1-5:2006. 2006: Brussels, Belgium.

[34] Gardner, L. and Yun, X. Description of stress-strain curves for cold-formed steels. Construction and Building Materials, 2018. 189: 527-538. https://doi.org/10.1016/j.conbuildmat.2018.08.195

[35] Zhu, A.Z., Zhu, H.P., Zhang, X.W., and Lu, Y. Experimental study and analysis of inner-stiffened cold-formed SHS steel stub columns. Thin-Walled Structures, 2016. 107: 28-38. https://doi.org/10.1016/j.tws.2016.04.026

[36] Key, P.W. and Hancock, G.J. Hancock, A theoretical investigation of the column behaviour of cold-formed square hollow sections. Thin-Walled Structures, 1993. 16(1-4): 31-64. .https://doi.org/10.1016/0263-8231(93)90040-H

[37] Valiente, A. Fracture and fatigue failure in the Spanish codes for design of steel structures. Engineering Failure Analysis, 2009. 16(8): 2658-2667. https://doi.org/10.1016/j.engfailanal.2009.04.025

[38] Somodi, B. and Kovesdi, B. Residual stress measurements on cold-formed HSS hollow section columns. Journal of Constructional Steel Research, 2017. 128: 706-720. https://doi.org/10.1016/j.jcsr.2016.10.008

[39] Gardner, L., Saari, N. and Wang, F. Comparative experimental study of hot-rolled and cold-formed rectangular hollow sections. Thin-Walled Structures, 2010. 48(7): 495-507. https://doi.org/10.1016/j.tws.2010.02.003

[40] Hu, S.D., Ye, B. and Li, L.X. Materials properties of thick-wall cold-rolled welded tube with a rectangular or square hollow section. Construction & Building Materials, 2011. 25(5): 2683-2689. https://doi.org/10.1016/j.conbuildmat.2010.12.019

[41] Sun, M., and Packer, J.A. Direct-formed and continuous-formed rectangular hollow sections-Comparison of static properties. Journal of Constructional Steel Research, 2014. 92: 67-78. .https://doi.org/10.1016/j.jcsr.2013.09.013

[42] Chen, J. Study of ultimate axial compressive capacity of cold-formed medium wall square and rectanglar hollow steel columns with initial imperfections. 2008, Wuhan University of Technology.

[43] Gao, H. Experimental research and FEM simulation of ultimate axial compression of cold-formed medium wall hollow steel columns. 2007, Wuhan University of Technology.